



Performance enhancement of perovskite/porous-Si photodetectors by reducing the dark current with concomitant use of graphene quantum dots in the active layer and bathocuproine on the back surface

Chan Wook Jang ^{a,1}, Dong Hee Shin ^{b,1}, Suk-Ho Choi ^{a,*}

^a Department of Applied Physics, Institute of Natural Sciences, and Integrated Education Institute for Frontier Science and Technology (BK21 Four), Kyung Hee University, Yongin 17104, South Korea

^b Department of Smart Sensor Engineering, Andong National University, Andong, Gyeongbuk 36729, South Korea



ARTICLE INFO

Article history:

Received 14 December 2022

Received in revised form 14 March 2023

Accepted 16 March 2023

Available online 17 March 2023

Keywords:

Porous Si
Perovskite
Graphene quantum dot
Heterostructure
Photodetector
Response time
Broadness

ABSTRACT

Reduction of dark current (DC) in perovskite photodetectors (PDs) is one of the major issues to improve their functionalities. In this work, we employ graphene quantum dots (GQDs), porous Si (PSi), and bathocuproine (BCP) in MAPbI₃-based PDs for enhancing the film crystallinity/photoresponse, the spectrum broadness/response speed, and the back-surface passivation/carrier blocking effect, respectively. The GQDs-added MAPbI₃ (MAPbI₃:GQDs)/PSi/BCP PD exhibits a delta-function-like photocurrent (PC)/DC ratio-vs-voltage behavior with a maximum of about 10⁵, resulting from sharp reduction of the DC and the built-in potential profile at 0 V, meaning "self-powered". Specific detectivity of the MAPbI₃:GQDs/PSi/BCP PD is almost 50 times larger than that of the counterpart without GQDs and BCP. The PD also shows a broadband photoresponse in the 380 – 950 nm range, where the responsivity ($R \geq 0.2 \text{ AW}^{-1}$), and decay time of 735 ns, extremely higher performance than the bulk-Si counterpart PD. The PD maintains 73 or 65% of its original PC even after 2000 h under 600-nm (600 μWcm^{-2}) or 1-sun (100 mWcm⁻²) illumination, respectively, indicating remarkable stability.

© 2023 Elsevier B.V. All rights reserved.

1. Introduction

Metal halide perovskites are very attractive for their optoelectronic device applications due to the excellent properties such as high absorption coefficient, long electron-hole diffusion length, small exciton binding energy, and so on [1–5]. Particularly, a lot of efforts have been made to develop highly-sensitive perovskites-based photodetectors (PDs) [6–12], whose spectrum broadness is limited in further extention, resulting from the fundamental band structure [13]. To overcome this problem, perovskite/Si heterostructures were employed for the bandgap engineering, thereby broadening the spectral range of the PD [14,15]. For example, the single-crystal (SC) MAPbBr₃/bulk Si heterojunction PDs offered broadband spectrum as well as fast photoresponse [15], but continued performance optimization and reproducibility enhancement are not so much available because the size control is difficult.

Therefore, another approach is needed to fabricate uniform and large SC grains. Moreover, there is a limit to improving the response time by using heterojunctions with bulk Si due to the inherent indirect bandgap nature of Si as shown in the previous literature [16–18]. On the other hand, nanostructured Si such as porous Si (PSi) has been utilized in photonic devices such as solar cells and PDs thanks to the high light absorption, high optical gain, and high surface-to-surface ratio. Especially, PSi PDs showed faster photoresponse than the bulk-Si PDs [19–21].

Considering the advantages of the two materials, perovskite and PSi for the optoelectronic device applications, perovskite/PSi heterostructure PDs are expected to exhibit high response speed as well as broad spectrum. In addition, graphene quantum dots (GQDs) are known to be well mixed with perovskite films for enhancing the film crystallinity [22–24], thereby decreasing dark current (DC) in perovskite PDs, and bathocuproine (BCP) layer was successfully employed for lowering the trap density at the Si/metal electrode interface, leading to DC reduction in perovskite solar cells [25].

In the last several years, a lot of studies have been done to reduce the DC in perovskite PDs by using various kinds of methods such as film crystallization [26], back-surface passivation [27,28], and carrier

* Corresponding author.

E-mail address: sukho@knu.ac.kr (S.-H. Choi).

¹ These authors have contributed equally to this study.

blocking [29–31], and so on. In this work, we greatly reduced DC of a MAPbI₃/PSi heterostructure PD by employing GQDs in the active layer and BCP on the back surface, resulting in the enhancement of the film crystallinity, trap passivation, and carrier blocking effect. For characterizing MAPbI₃/PSi heterostructure PDs with/without GQDs and/or BCP, we measured key figures of merit, such as photocurrent (PC)/DC ratio, responsivity (R), external quantum efficiency (EQE), specific detectivity (D*), sensitivity linearity, PC rise/decay times, and long-term stability.

2. Experimental section

2.1. Fabrication of MAPbI₃:GQDs/porous Si/Si/bathocuproine photodetectors

Au nanoparticles (NPs) were deposited on a clean 10-ohm-cm n-Si substrate by using metal sputtering for 5 s. Sequentially, the Au NPs/n-Si was immersed in a mixed solution of HF and H₂O₂ (volume ratio 1:1) for 5 s for etching to form randomly-oriented pores on the Si surface, and the residual Au NPs were then removed through aqua regia. The systematic process for the preparation of the PSi was more detailed in the previous literature [19–21]. To prepare the GQDs-added MAPbI₃ (MAPbI₃:GQDs), 10 mg/L GQDs were firstly dispersed in dimethylformamide (DMF). Secondly, a powder mixed with CH₃NH₃I and PbI₂ (molar ratio 1:1) was added to the DMF solution containing GQDs and was immediately dissolved at 60 °C. Finally, the MAPbI₃:GQDs solution was dropped on the entire surface of the PSi and then, spin coating was done continuously at 1000 rpm for 5 s and 5000 rpm for 15 s consecutively. To promote rapid nucleation, chlorobenzene was poured onto the substrate 5 s after the second spin coating, and the MAPbI₃:GQDs/PSi stack was then heated at 100 °C for 5 min. BCP dissolved in isopropyl alcohol (0.5 mg mL⁻¹) was dropped on the back side of Si and was spin-coated at 1500 rpm for 40 s. To complete the PD structure, Au and InGa selected considering the work function of the constituent materials were deposited on the front and rear electrodes, respectively. The active area of the PD was made to be 0.09 and 0.25 cm².

2.2. Characterizations

The surface of the PSi and the cross-sectional structure of the perovskite/PSi heterojunction were characterized by field emission scanning electron microscopy (FE-SEM, Carl Zeiss, model LEO SUPRA 55). Analysis of the size and distribution of GQDs was performed by electron energy loss spectroscopy (EELS) mapping and high-resolution transmission electron microscopy (HRTEM, JEOL JEM-2100 F). Photoluminescence (PL) and time-resolved PL (TRPL) measurements on the perovskite films without/with GQDs were recorded using 532 continuous-wave and pulsed lasers, respectively. Raman spectra of the PSi and GQDs were obtained by using a Raman spectrometer system with a 532 nm laser line. Transmittance and absorbance of the perovskite films without/with GQDs were measured using ultra-violet (UV)-visible (Vis) near-infrared spectroscopy (Agilent Varian, Carry 5000). Electrical characterization of the PD was done in a semiconductor parameter analyzer system (Keithley 2400). The sensitivity of a Si photodiode in the wavelength (λ) range of 300–1100 nm was calibrated to characterize the spectral response of the PD by using a 450 W xenon light source and a monochromator. The light sensitivity linearity of the PD was evaluated by systematically adjusting the light intensity (I_0) of a 600-nm laser with a neutral-density filter. The rise/decay times of the photoresponse were recorded using a 532-nm pulse laser with a frequency of 0.2 MHz. The DC noise of the PD was measured in the dark by using a current preamplifier (Stanford Research Systems, SR570) and a dynamic signal analyzer (Agilent, 35670 A).

3. Results and discussion

High-porosity PSi was shown to be formed on a Si wafer during the etching process by FE-SEM (Supporting Information, Fig. S1a-b). The Raman peak of the PSi was shifted to a lower wavenumber with its full width at half maximum (FWHM) being widened, compared to bulk Si (Supporting Information, Fig. S1c), consistent with previous results [32], further demonstrating well formation of the PSi. The average diameter of GQDs was estimated to be ~5 nm by TEM evaluation of their dispersion and distribution (Supporting Information, Fig. S2a). The EELS spectrum of GQDs was peaked at ~285 and ~291 eV, corresponding to π^* and σ^* states [22,32], respectively, (Supporting Information, Fig. S2b) and the D and G bands of graphene [22,32] are clearly seen in the Raman spectrum of GQDs (Supporting Information, Fig. S2c), indicating their high-quality.

The surface structure of perovskite films without/with GQDs was characterized by FE-SEM. Crystalline grains in perovskites tend to grow independently centering around large number of nucleation sites, resulting in the reduction of their average size [22–24]. Perovskite films without GQDs consisted of relatively-small grains with their size ranging from 50 to 200 nm (Supporting Information, Fig. S3a), whereas the size of the crystals increased to ~400 nm by adding the GQDs (Supporting Information, Fig. S3b). Since the bond between GQDs and PbI₂ is weaker than that between MAI and PbI₂, GQDs are repelled during the formation of MAPbI₃ [33]. In this work, the GQDs are believed to finally aggregate at the grain boundaries once the growth of the perovskite grains is completed. The increase in the grain size by including the GQDs can be explained by two main reasons, as follows. The unshared electrons of -OH and -COOH belonging to the GQDs can slow down the crystallization by interacting with PbI₂ [34,35]. In addition, incorporation of the water present in the GQDs solution within DMF results in a growth of perovskites due to the lower boiling point and the higher vapor pressure of water compared to DMF [36]. As a result, larger crystals can be formed in the perovskite films by the inclusion of the GQDs.

Raman spectra of the MAPbI₃ films with/without GQDs were seen at around 110 cm⁻¹ (Supporting Information, Fig. S3c), originating from the MAPbI₃ [37]. Only the MAPbI₃:GQDs sample showed the D and G bands of GQDs at 1361 and 1595 cm⁻¹, respectively, indicating the successful incorporation of GQDs into the MAPbI₃ matrix. As shown in the X-ray diffraction (XRD) spectrum (Supporting Information, Fig. S3d), the (110) and (220) crystalline peaks of MAPbI₃ [38] were clearly seen regardless of the presence of GQDs, indicating almost no variation in the tetragonal structure. Particularly, the (110) XRD peak was changed to be higher and narrower, by adding the GQDs in the perovskite film, judging from its intensity and FWHM, indicating better crystallinity, consistent with the SEM results.

UV-Vis absorbance/transmittance spectra were obtained in the range of 300–1050 nm for the perovskite films with/without GQDs (Supporting Information, Fig. S3e). Due to the influence of the GQDs, the absorbance and transmittance of the film slightly increased and decreased, respectively. The PL was peaked at 785 nm, irrespective of the existence of GQDs (Supporting Information, Fig. S3f), as shown previously [22,23]. The PL intensity was greatly weakened after adding the GQDs in the perovskite film. The carrier lifetime was calculated by measuring the TRPL of the MAPbI₃ films without/with GQDs (Supporting Information, Fig. S3g). The lifetime was shortened from 9.87 to 1.98 ns by the inclusion of the GQDs. The PL quenching/lifetime reduction means less carrier recombination, thereby facilitating more-efficient charge extraction/transfer. In other words, the addition of GQDs to the perovskite film is very useful for enhancing the transport of the photo-induced carriers, resulting in better photoresponse.

Fig. 1(a) shows a schematic and a real image of a typical MAPbI₃:GQDs/PSi/BCP PD. Here, the illumination is directed towards the

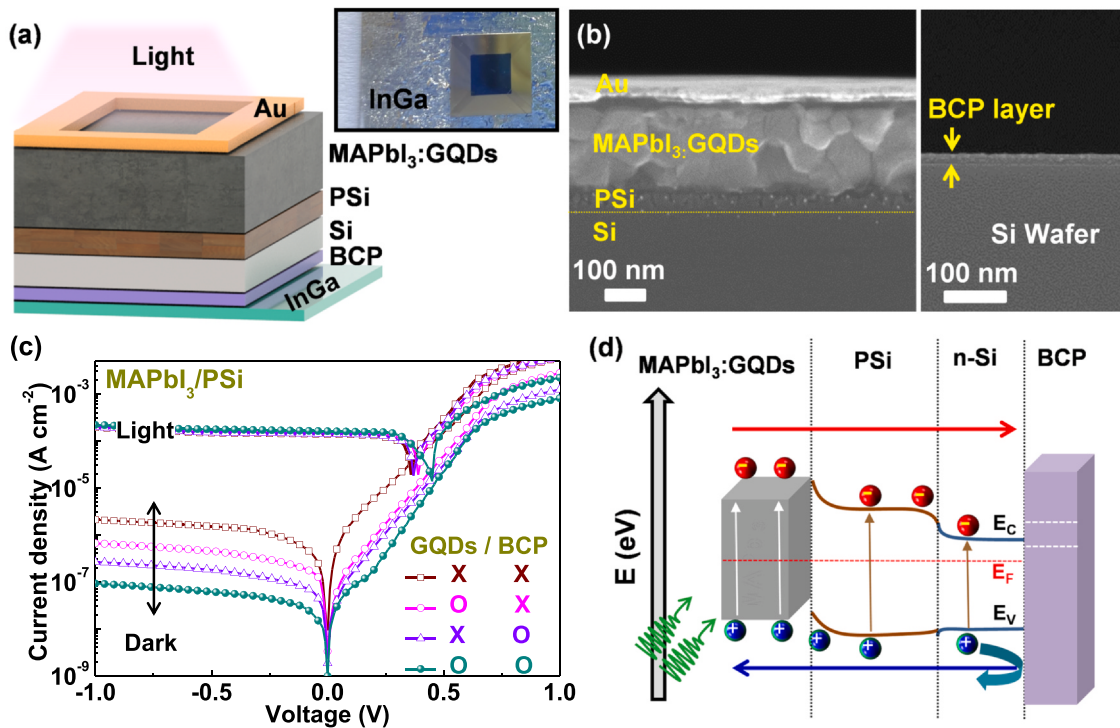


Fig. 1. (a) Schematic device architecture/real image and (b) cross-sectional FE-SEM images of a typical MAPbI₃:GQDs/PSi/Si/BCP PD with Au/InGa top/bottom electrodes. (c) Dark photo-J-V curves of the MAPbI₃/PSi/Si PDs without GQDs and BCP, with only GQDs, and with GQDs and BCP. (d) Energy band diagram of the MAPbI₃:GQDs/PSi/Si/BCP PD. The marking "O" or "X" indicates that a particular layer is included in the device structure or not, respectively.

side of the perovskite film. The FE-SEM image in Fig. 1(b) shows a clear separation of the constituent layers in the completed PD. Fig. 1(c) shows current density-voltage (J-V) behaviors of the PDs with/without GQDs and/or BCP under dark as well as under illumination. By adding the GQDs in the MAPbI₃ layer, the DC is reduced over the full range of bias. The leakage current resulting from the charge carriers trapped in crystallographic defects of perovskites are one of the major factors to increase the DC in perovskite PDs [26]. This explains why the DC decreases due to the enhancement of the crystallinity, caused by the GQDs mixed in the active layer, as shown above (Supporting Information, Fig. S3a, b & d). The DC of the PD exhibits a sharp deep at 0 V, as shown in Fig. 1(c), resulting from the high energy barrier formed at the MAPbI₃/PSi interface for the electrons in the MAPbI₃ to get over to go to the PSi, as shown in Fig. 1(d). As the reverse bias ($V_a < 0$) increases, the DC increases because the MAPbI₃/PSi interface barrier is lowered due to the upward movement of the Fermi level of the MAPbI₃. Under forward bias ($V_a > 0$), the barrier heights at the MAPbI₃/PSi and PSi/n-Si interfaces are reduced, resulting in the increase of the DC as the voltage increases.

The BCP layer is known to act as a surface planarizer leading to a reduction of roughness which improves the Si/metal electrode interface by lowering the interface trap density, resulting in the DC decrease under reverse bias as well as under forward bias, as shown in previous publication [25]. In this report, it was also demonstrated that the magnitude of the DC strongly depends on the trap density of the BCP film, controlled by changing the preparation condition. This effect was more effective under reverse bias, thereby increasing the rectification ratio, consistent with the dark J-V curves of the PDs with the BCP, as shown in Fig. 1(c). The ideality factor (n) was evaluated from the dark J-V curves (Supporting Information, Fig. S4) based on the following formula: $J = J_s [\exp(eV/nk_B T) - 1]$ [39], where J_s is the ideal reverse saturation current density, k_B is the Boltzmann's constant, and T is the temperature. The n value extracted from the slopes were 2.39, 1.91, 1.86, and 1.78 for the PDs without

GQDs and BCP, with only GQDs, with only BCP, and with GQDs and BCP, indicating better diode quality by the inclusion of GQDs and/or BCP in the active layer.

On the other hand, the current variation under illumination is almost negligible, irrespective of the existence of the GQDs and/or BCP, as shown in Fig. 1(c). The GQDs increase the light absorption of the film, as shown above (Supporting Information, Fig. S3e), thereby producing higher-density electron-hole pairs. The BCP layer can act as an energy barrier for blocking the flow of the photo-induced electrons and holes, thereby reducing the current. The electron-hole pairs are generated in all the constituent materials of the GQDs-added MAPbI₃, PSi, and n-Si during illumination, which affects the magnitude of the current in both bias directions. The BCP layer is also known to be useful for suppressing the electron-hole recombination at the n-Si/InGa interface [19], as indicated in Fig. 1(d), thereby facilitating the flow of the photo-induced carriers, resulting in the increase of the PC (also the current, \because current = DC + PC). Especially, the DC level is very high at large forward bias ($V_a >$ about +0.3 V), as shown in Fig. 1(c), which makes the PC variation less sensitive in this region. All of these combined trade-off effects possibly explain why the negligible variation in the current under illumination occurs, irrespective of the insertion of the GQDs and/or BCP.

Based on the above results, the photoresponse of the PDs was further evaluated at 0 bias, i.e., under "self-powered" condition. Fig. 2(a) exhibits delta-function-like PC/DC ratio-vs- V_a behaviors, resulting from the negligible DC (Fig. 1(c)) and the built-in potential profile at 0 V (Fig. 1(d)). The PC/DC ratio is maximized to about 10⁵ by adding the GQDs in the MAPbI₃ and the BCP on the back surface. In other words, the PD can be well operated even at zero voltage, thereby reducing the power consumption. Fig. 2(b) shows spectral R of the PDs, obtained by the equation: $R = PC/I_L$ [40]. The MAPbI₃:GQDs/PSi/BCP PD shows a broadband photoresponse in the 380–950 nm where $R \geq 0.2$ AW⁻¹ whilst the spectrum broadness in the counterpart: MAPbI₃:GQDs/bulk-Si/BCP PD is reduced to the 400–

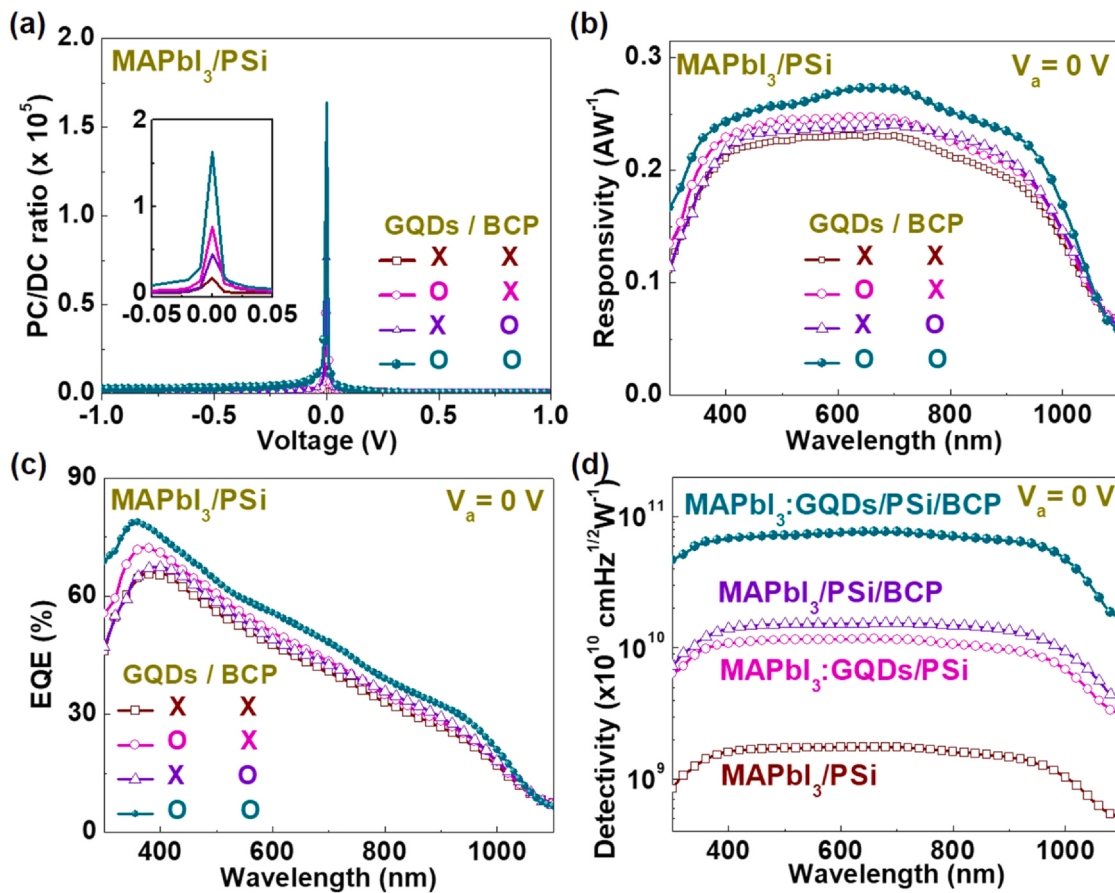


Fig. 2. (a) Photocurrent/dark current (PC/DC) ratios as functions of bias voltage and (b) spectral responsivities/(c) external quantum efficiencies/(d) detectivities at 0 V for the MAPbI₃/PSi PDs with/without GQDs and/or BCP at a bias of 0 V. The marking "O" or "X" indicates that a particular layer is included in the device structure or not, respectively.

Table 1

Performance comparison of the MAPbI₃:GQDs/PSi/n-Si/BCP PDs with other perovskite- or Si-based hybrid PDs previously-reported in literatures.

Device Structure	Self-powered	R (AW ⁻¹)	D* (cmHz ^{1/2} W ⁻¹)	Rise/decay time [ms/ms]	Ref
MAPbBr ₃ SC/Si	X	0.14	5.9 × 10 ¹⁰	5 × 10 ⁻⁴ /2 × 10 ⁻³	15
Graphene/h-BN/Si	O	0.11	2.8 × 10 ¹⁰	9 × 10 ⁻¹ /1	16
Graphene/WS ₂ /Si	X	9 × 10 ⁴	8.9 × 10 ¹¹	9 × 10 ⁻¹ /2	17
Graphene/Gd ₃ Fe ₅ O ₁₂ /Si	X	0.9	1.3 × 10 ¹³	2 × 10 ⁻² /2 × 10 ⁻²	18
TFSA-graphene/h-BN/PSi/ n-Si/BCP	O	0.58	1 × 10 ¹¹	8 × 10 ⁻³ /2 × 10 ⁻²	19
Graphene/Si nanowire	O	0.15	1.4 × 10 ¹²	2 × 10 ⁻³ /3 × 10 ⁻³	41
WS ₂ -ZnO/Si	O	9.8	1 × 10 ¹²	1 × 10 ² /2 × 10 ²	42
chlorophyll-b/Si nanowire	O	0.73	2.2 × 10 ¹²	10 ³ /10 ³	43
TFSA-graphene/GQDs/ SiQDs:SiO ₂ /n-Si	O	0.67	8.4 × 10 ¹²	9 × 10 ⁻⁴ /1 × 10 ⁻³	44
PEDOT:PSS/Si nanowire	O	1 × 10 ³	5.8 × 10 ¹³	4 × 10 ⁻¹ /4 × 10 ⁻¹	45
MAPbI ₃ /MoS ₂	O	0.06	-	356/204	46
MAPbI ₃ /WS ₂	X	2.3	2 × 10 ¹²	3/8	47
MAPbI ₃ /WSe ₂	X	100	2 × 10 ¹¹	85/3 × 10 ³	48
Triple cation perovskite/MoS ₂	X	342	1.1 × 10 ¹²	27/32	49
CsPbBr ₃ /MoS ₂	X	24	1.1 × 10 ¹²	5 × 10 ⁻³ /2 × 10 ⁻²	50
Cs ₂ AgBiBr ₆ /WS ₂ /graphene	O	0.05	1.5 × 10 ¹³	5 × 10 ⁻² /5 × 10 ⁻²	51
Graphene/(PEA) ₂ SnI ₄ / MoS ₂ /graphene	O	0.12	8.1 × 10 ⁹	34/38	52
MAPbBr ₃ /N-rGO	X	3 × 10 ⁴	10 ¹²	30/10 ²	53
Carbon Nanotube/MAPbI _x Br _{3-x}	X	0.06	3.8 × 10 ¹²	7 × 10 ⁻³ /1 × 10 ⁻²	54
PdSe ₂ /FA _{0.85} Cs _{0.15} PbI ₃	O	0.31	10 ¹³	3 × 10 ⁻³ /4 × 10 ⁻³	55
MAPbI ₃ /PbSe	X	0.23	4 × 10 ¹²	4 × 10 ⁻³ /3 × 10 ⁻²	56
MAPbI ₃ :GQDs/PSi/Si/BCP	O	0.2	7.6 × 10 ¹⁰	1 × 10 ⁻³ /2 × 10 ⁻³	This work

800 nm range (Supporting Information, Fig. S5). As shown in Fig. 2(c), the spectral EQE was determined by the following formula: $\text{EQE} = (hc/q)(1/\lambda)R$, where h is Planck constant, c is the velocity of light, and q is the electron charge. Unlike the flat shape of the R spectrum, the EQE is enhanced in the small λ range, originating from the format of the EQE formula.

Among the figures of merit for evaluating a PD, noise equivalent power (NEP), meaning the minimum detectable power, and D^* were calculated from the formula: $\text{NEP} = I_n/R = (A\Delta f)^{1/2}/D^*$ [39], where I_n is the noise current (Supporting Information, Fig. S6a), A is the absorption area (0.25 cm^2), and f is the electrical bandwidth in the frequency range from 1 to 10 kHz. The minimum/maximum of NEP/ D^* are $6.55 \text{ pW Hz}^{-1/2}/7.63 \times 10^{10} \text{ cmHz}^{1/2} \text{ W}^{-1}$, respectively for the $\text{MAPbI}_3:\text{GQDs/PSi/BCP}$ PD, as shown in Fig. 2(d) (Supporting Information, Fig. S6b). These results are comparable to those of previously-reported perovskite- or Si-based hybrid PDs, as summarized in Table 1 [15–17,19,41–44,47–50,52,53,56].

Fig. 3(a) shows periodic on/off photoresponse of the $\text{MAPbI}_3:\text{GQDs/PSi/BCP}$ PD, measured as a function of I_L under continuous illumination at 600 nm. Here, the PC density was measured by varying the I_L from 10^{-8} to $10^{-3} \text{ W cm}^{-2}$. Using the PC density- I_L plot, as shown in Fig. 3(b), α was calculated to be 0.88 by the following equation: $\text{PC} \propto I_L^\alpha$ [32], where α is a parameter closely related to the recombination process of the photoexcited carriers, indicating optimized formation of the active layer in the PD by defect engineering. Linear dynamic range (LDR) is defined as the illuminance range over which the PD's current response to the I_L scales linearly. Larger LDR means excellent functionality in a wide range of light power. The LDR is calculated to be 80 dB by the following equation: $\text{LDR} = 20 \log (J_{ph}^*/J_d)$, where J_{ph}^* is the PC density measured at a luminance of 1 mWcm^{-2} and J_d is DC density. Fig. 3(c) shows a good linearity of the R as a function of I_L with a maximum being 0.84 AW^{-1} at $I_L = 36 \text{ nWcm}^{-2}$, which can be attributed to the improved photocarrier recombination rate, caused by the inclusion of the GQDs and BCP.

Fig. 4(a) shows PC transient behaviors of the $\text{MAPbI}_3:\text{GQDs/PSi/BCP}$ PDs with 0.09 and 0.25 cm^2 active area, measured by using a 532 nm pulse laser with a frequency of 0.2 MHz. The rise/decay times of the smaller PD are 654/735 ns whilst those of the larger PD are 1558 ns/1739 ns. So, the larger the area of the PD, the longer the times, possibly governed by the RC constant of the circuit [57]. These rise/decay are much faster compared to the counterpart: $\text{MAPbI}_3:\text{GQDs/bulk-Si/BCP}$ PD (Supporting Information, Fig. S5c), and comparable to or even better than those of previously-reported perovskite- or Si-based hybrid PDs [15–19,41–56]. The frequency at which the photoresponse power is one half of the initial value is called as the cutoff frequency, which is a criterion for evaluating the frequency response. The 3 dB bandwidths in the frequency-dependent R curve are 1226 and 545 kHz for 0.09 and 0.25 cm^2 PDs, respectively, as shown in Fig. 4(b), consistent with the area-dependent decay times, as shown in Fig. 4(a).

We also studied long-term stability of the $\text{MAPbI}_3:\text{GQDs/PSi/BCP}$ PD. The PD was stored under atmosphere at 25°C temperature and 30% humidity. Fig. 5(a) shows repeated on/off photoresponse performance of the PD under dark as well as under 600-nm ($I_L: 600 \mu\text{Wcm}^{-2}$) illumination during 500, 1000, 1500, and 2000 h (see Supporting Information, Fig. S7a for 1-sun ($I_L: 100 \text{ mWcm}^{-2}$) illumination) The PD retained 73/65% of its original PC even after 2000-h 600-nm/1-sun illumination, respectively, indicating remarkable stability, as summarized in Fig. 5(b) (and Supporting Information, Fig. S7b).

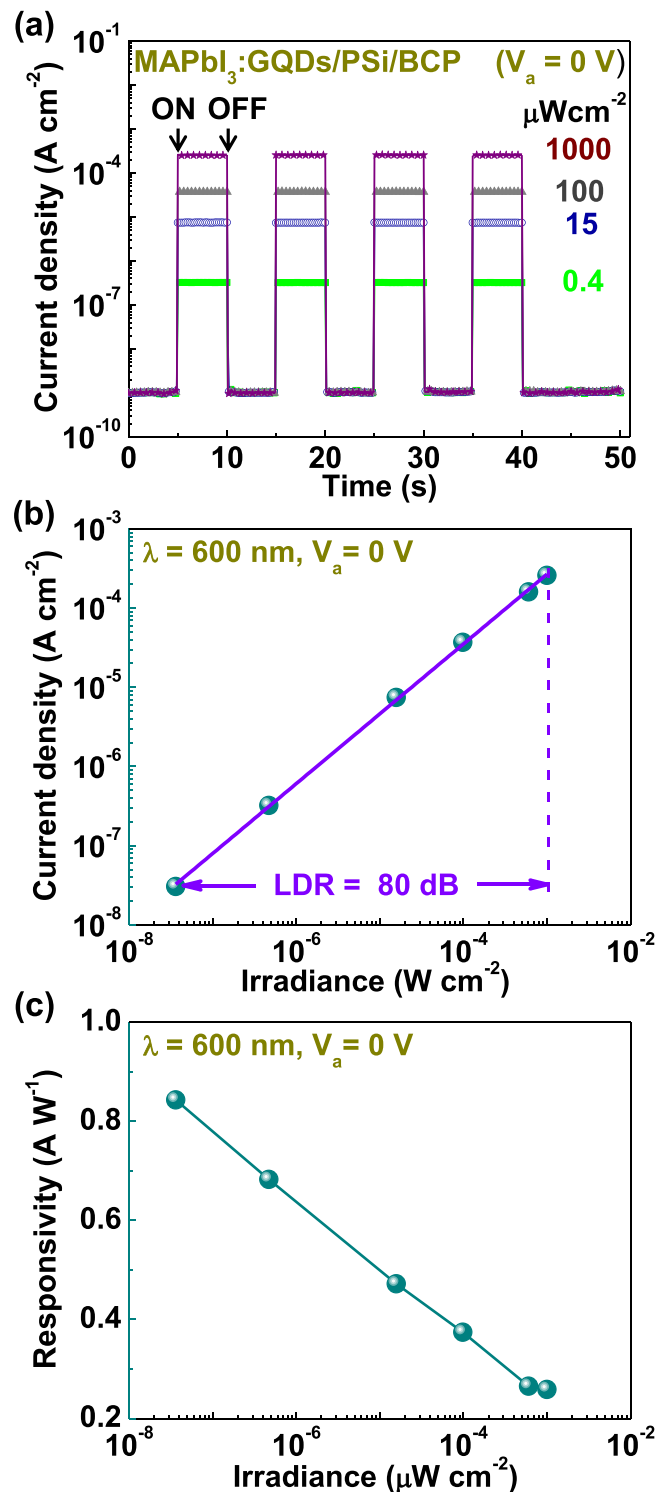


Fig. 3. (a) Regular and reversible on/off photocurrent switching curves of $\text{MAPbI}_3:\text{GQDs/PSi/BCP}$ PD for various light powers at $\lambda = 600 \text{ nm}$. Here, the voltage bias is fixed at 0 V. (b) Current density and (c) responsivity of the PD as functions of light power (I_L) at a bias of 0 V.

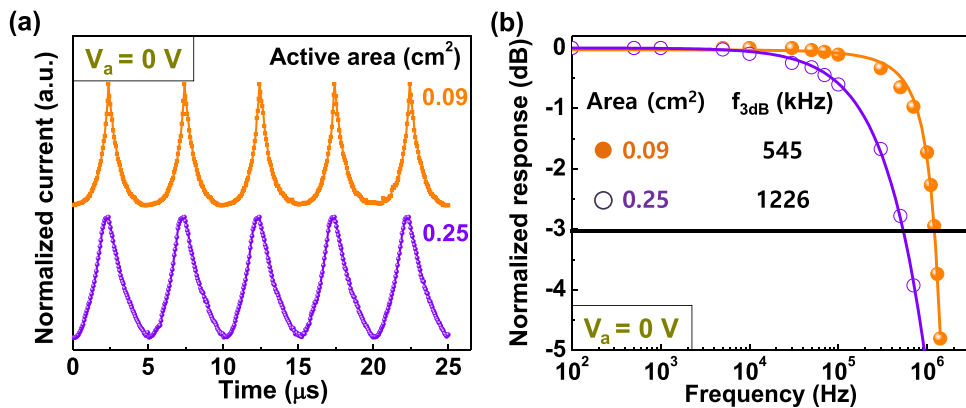


Fig. 4. (a) Normalized repetitive on/off transient photocurrent switching behaviors at a pulse frequency of 0.2 MHz for the PDs with 0.09 and 0.25 cm² active area. (b) Normalized response as functions of pulse frequency for the PDs with 0.09 and 0.25 cm² active area. Here, the applied voltage was fixed at V_a = 0 V.

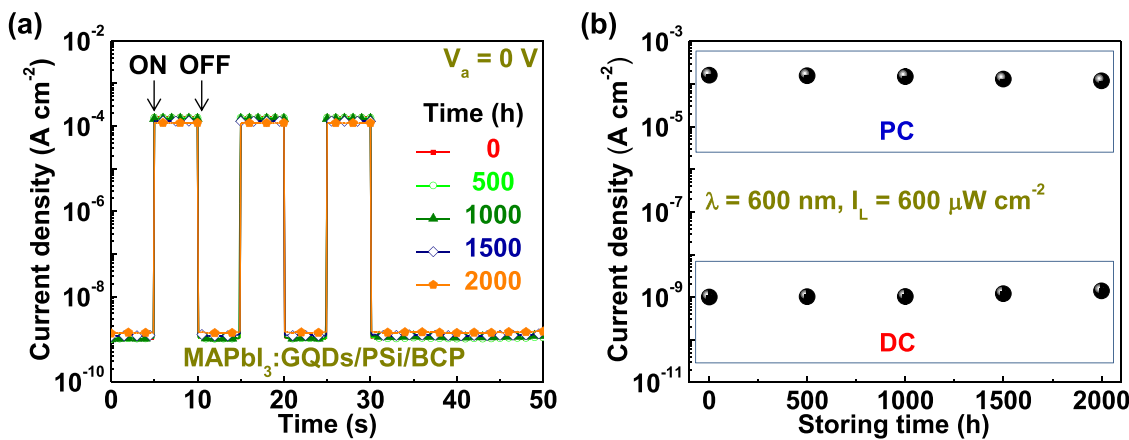


Fig. 5. Long-term stability characteristics of a typical MAPbI₃:GQDs/PSi/Si/BCP PD under 600-nm illumination. Temporal change of (a) the repeated on/off current switching curves and (b) the PC/DC under ambient conditions for 2000 h.

4. Conclusions

Use of the MAPbI₃/PSi heterostructure was successful for enhancing the spectrum broadness and response speed of perovskite-based PDs. The spectrum/decay time were further extended/shortened to the 380 – 950 nm range and 735 ns, respectively by employing GQDs in the active layer and BCP on the back surface. The DC of the MAPbI₃:GQDs/PSi/BCP PD was negligible at 0 V, meaning “self-powered”, thereby showing a delta-function-like PC/DC ratio-vs-V_a behavior with a maximum of about 10⁵, resulting in about 50 times enhancement of D*, compared to the MAPbI₃/PSi PD. These performances, extremely higher than those of the bulk-Si counterpart PD, were attributed to the increased crystallinity of the active layer and the effective carrier blocking effect, caused by the inclusion of GQDs and BCP. The PC of the PD was maintained at 73/65% of its original value even after 2000-h 600-nm/1-sun illumination, respectively, meaning excellent stability.

CRediT authorship contribution statement

C. W. Jang and D. H. Shin performed device design, device fabrication, and characterization for the photodetectors. S.-H.C. initiated, supervised the work, and wrote the paper. All authors discussed the results and commented on the manuscript.

Data Availability

Data will be made available on request.

Declaration of Competing Interest

The authors declare that they have no known competing financial interests or personal relationships that could have appeared to influence the work reported in this paper.

Acknowledgments

This work was supported by the National Research Foundation of Korea (NRF) grant funded by the Korea government (MSIT) (No. RS-2023-00208310).

Appendix A. Supporting information

Supplementary data associated with this article can be found in the online version at doi:10.1016/j.jallcom.2023.169716.

References

- [1] A.G. Ricciardulli, S. Yang, J.H. Smet, M. Saliba, Emerging perovskite monolayers, *Nat. Mater.* 20 (2021) 1325–1336.

- [2] A.D. Marshall, J. Acharya, G. Alkhalifah, B. Kattel, W.-L. Chan, J.Z. Wu, Probing the origin of light-enhanced ion diffusion in halide perovskites, *ACS Appl. Mater. Interfaces* 13 (2021) 33609–33617.
- [3] F. Ruf, M.F. Aygüler, N. Giesbrecht, B. Rendenbach, A. Magin, P. Docampo, H. Kalt, M. Hetterich, Temperature-dependent studies of exciton binding energy and phase-transition suppression in (Cs,FA,MA)Pb(I,Br)₃ perovskites, *APL Mater.* 7 (2019) 031113.
- [4] X. Chen, H. Lu, K. Wang, Y. Zhai, V. Lunin, P.C. Sercel, M.C. Beard, Tuning spin-polarized lifetime in two-dimensional metal-halide perovskite through exciton binding energy, *J. Am. Chem. Soc.* 143 (2021) 19438–19445.
- [5] S. Mannar, P. Mandal, A. Roy, R. Viswanatha, Experimental determination of the molar absorption coefficient of cesium lead halide perovskite quantum dots, *J. Phys. Chem. Lett.* 13 (2022) 6290–6297.
- [6] J. He, J. Su, J. Di, Z. Lin, S. Zhang, J. Ma, J. Zhang, S. Liu, J. Chang, Y. Hao, Surface reconstruction strategy improves the all-inorganic CsPbIBr₂ based perovskite solar cells and photodetectors performance, *Nano Energy* 94 (2022) 106960.
- [7] D. Hao, D. Liu, Y. Shen, Q. Shi, J. Huang, Air-stable self-powered photodetectors based on lead-free CsBi_{1/10}SnO₂ heterojunction for weak light detection, *Adv. Funct. Mater.* 31 (2021) 2100773.
- [8] J. Tao, Z. Xiao, J. Wang, C. Li, X. Sun, F. Li, X. Zou, G. Liao, Z. Zou, A self-powered, flexible photodetector based on perovskite nanowires with Ni-Al electrodes, *J. Alloy. Compd.* 845 (2020) 155311.
- [9] V.O. Eze, G.R. Adams, L.B. Carani, R.J. Simpson, O.I. Okoli, Enhanced inorganic CsPbIBr₂ perovskite film for a sensitive and rapid response self-powered photodetector, *J. Phys. Chem. C* 124 (2020) 20643–20653.
- [10] C. Li, H. Wang, F. Wang, T. Li, M. Xu, H. Wang, Z. Wang, X. Zhan, Ultrafast and broadband photodetectors based on a perovskite/organic bulk heterojunction for large-dynamic-range imaging, *Light: Sci. Appl.* 9 (2020) 31.
- [11] H. Nguyen, T.M.S. Kim, C.W. Bark, Solution-processed and self-powered photodetector in vertical architecture using mixedhalide perovskite for highly sensitive UVC detection, *J. Mater. Chem. A* 9 (2021) 1269–1276.
- [12] Z. Rao, W. Liang, H. Huang, J. Ge, W. Wang, S. Pan, High sensitivity and rapid response ultraviolet photodetector of a tetragonal CsPbCl₃ perovskite single crystal, *Opt. Mater. Express* 10 (2020) 1374–1382.
- [13] Q. Ou, X. Bao, Y. Zhang, H. Shao, G. Xing, X. Li, L. Shao, Q. Bao, Band structure engineering in metal halide perovskite nanostructures for optoelectronic applications, *Nano Mater. Sci. I* (2019) 268–287.
- [14] Z. Zhang, C. Xu, C. Zhu, X. Tong, C. Fu, J. Wang, Y. Cheng, L. Luo, Fabrication of MAPbI₃ perovskite/Si heterojunction photodetector arrays for image sensing application, *Sens. Actuator A-Phys.* 332 (2021) 113176.
- [15] X. Geng, F. Wang, H. Tian, Q. Feng, H. Zhang, R. Liang, Y. Shen, Z. Ju, Y.G.-N. Gou, Deng, J. Y.-t. Li, D. Ren, Y. Xie, T.-L. Yang, Ren, , Ultrafast photodetector by integrating perovskite directly on silicon wafer, *ACS Nano* 14 (2020) 2860–2868.
- [16] Y. Won, U.H. Lee, B.R. Kim, Y. Kang, T.W.I. Lee, E. Kim, J.H. Lee, Y.W.J. Yu, Efficient photovoltaic effect in graphene/h-BN/silicon heterostructure self-powered photodetector, *Nano Res.* 14 (2021) 1967–1972.
- [17] T. He, C. Lan, S. Zhou, Y. Li, Y. Yin, C. Li, Y. Liu, Enhanced responsivity of a graphene/Si-based heterostructure broadband photodetector by introducing a WS₂ interfacial layer, *J. Mater. Chem. C* 9 (2021) 3846–3853.
- [18] P. Ji, S. Yang, Y. Wang, K. Li, Y. Wang, H. Suo, T. Woldu, Y.X. Wang, F. Wang, L. Zhang, Z. Jiang, High-performance photodetector based on an interface engineering-assisted graphene/silicon Schottky junction, *Microsyst. Nanoeng.* 6 (2020) 9362.
- [19] C.W. Jang, D.H. Shin, S.-H. Choi, Bifunctional enhancement of photodetection and photovoltaic parameters in graphene/porous-Si heterostructures by employing interfacial hexagonal boron nitride and bathocuproine back-surface passivation layers, *J. Mater. Chem. C* 10 (2022) 15913–15919.
- [20] C.W. Jang, D.H. Shin, S.-H. Choi, High-photoresponse and broad-band graphene/WS₂/porous-Si heterostructure photodetectors, *ACS Appl. Nano Mater.* 5 (2022) 13260–13266.
- [21] J.H. Kim, D.H. Shin, H.S. Lee, C.W. Jang, J.M. Kim, S.W. Seo, S. Kim, S.-H. Choi, Enhancement of efficiency in graphene/porous silicon solar cells by co-doping graphene with gold nanoparticles and bis(trifluoromethanesulfonyl)-amide, *J. Mater. Chem. C* 5 (2017) 9005–9011.
- [22] D.H. Shin, S.H. Shin, S.G. Lee, S. Kim, S.-H. Choi, High-detectivity/-speed flexible and self-powered graphene quantum dots/perovskite photodiodes, *ACS Sustain. Chem. Eng.* 7 (2019) 19961–19968.
- [23] C.W. Jang, D.H. Shin, S.-H. Choi, Photostable electron-transport-layer-free flexible graphene quantum dots/perovskite solar cells by employing bathocuproine interlayer, *J. Alloy. Compd.* 886 (2021) 161355.
- [24] J. Zhang, T. Tong, L. Zhang, X. Li, H. Zou, J. Yu, Enhanced performance of planar perovskite solar cell by graphene quantum dot modification, *ACS Sustain. Chem. Eng.* 6 (2018) 8631–8640.
- [25] S. Castro-Hermosa, L. Wouk, I.S. Bicalho, L. d Q. Corrêa, B. d Jong, L. Cinà, T.M. Brown, D. Bagnis, Efficient fully blade-coated perovskite solar cells in air with nanometerthick bathocuproine buffer layer, *Nano Res.* 14 (2021) 1034–1042.
- [26] M. Ahmadi, T. Wu, B. Hu, A review on organic-inorganic halide perovskite photodetectors: Device engineering and fundamental physics, *Adv. Mater.* 29 (2017) 1605242.
- [27] Y. Shao, Z. Xiao, C. Bi, Y. Yuan, J. Huang, Origin and elimination of photocurrent hysteresis by fullerene passivation in CH₃NH₃PbI₃ planar heterojunction solar cells, *Nat. Commun.* 5 (2014) 5784.
- [28] P. Zhao, B.J. Kim, H.S. Jung, Passivation in perovskite solar cells: A review, *Mater. Today Energy* 7 (2018) 267–286.
- [29] S. Yoon, J. Cho, K.M. Sim, J. Ha, D.S. Chung, Low dark current inverted organic photodiodes using anionic polyelectrolyte as a cathode interlayer, *Appl. Phys. Lett.* 110 (2017) 083301.
- [30] S. Xiong, L. Li, F. Qin, L. Mao, B. Luo, Y. Jiang, Z. Li, J. Huang, Y. Zhou, Universal strategy to reduce noise current for sensitive organic photodetectors, *ACS Appl. Mater. Interfaces* 9 (2017) 9176–9183.
- [31] R. Ollearo, J. Wang, M.J. Dyson, C.H. Weijtens, M. Fattori, B.T. van Gorkom, A.J.J.M. van Breemen, S.C.J. Meskers, R.A.J. Janssen, G.H. Gelinck, Ultralow dark current in near-infrared perovskite photodiodes by reducing charge injection and interfacial charge generation, *Nat. Commun.* 12 (2021) 7277.
- [32] D.H. Shin, S.H. Shin, S. Kim, S.-H. Choi, High-performance and -stability graphene quantum dots-mixed conducting polymer/porous Si hybrid solar cells with titanium oxide passivation layer, *Nanotechnology* 31 (2020) 095202.
- [33] Y. Ma, H. Zhang, Y. Zhang, R. Hu, M. Jiang, R. Zhang, H. Lv, J. Tian, L. Chu, J. Zhang, Q. Xue, H.-L. Yip, R. Xia, X. Li, W. Huang, Enhancing the performance of inverted perovskite solar cells via grain boundary passivation with carbon quantum dots, *ACS Appl. Mater. Interfaces* 11 (2019) 3044–3052.
- [34] X. Zheng, Y. Deng, B. Chen, H. Wei, X. Xiao, Y. Fang, Y. Lin, Z. Yu, Y. Liu, Q. Wang, J. Huang, Dual functions of crystallization control and defect passivation enabled by sulfonic zwitterions for stable and efficient perovskite solar cells, *Adv. Mater.* 30 (2018) 1803428.
- [35] J.W. Lee, H.S. Kim, N. Park, Lewis acid-base adduct approach for high efficiency perovskite solar cells, *Acc. Chem. Res.* 49 (2016) 311–319.
- [36] X. Gong, M. Li, X.-B. Shi, H. Ma, Z.-K. Wang, L.-S. Liao, Controllable perovskite crystallization by water additive for high-performance solar cells, *Adv. Funct. Mater.* 25 (2015) 6671–6678.
- [37] A. Subramanian, J. Akram, S. Hussain, J. Chen, K. Qasim, W. Zhang, W. Lei, High-performance photodetector based on a graphene quantum dot/CH₃NH₃PbI₃ perovskite hybrid, *ACS Appl. Electron. Mater.* 2 (2020) 230–237.
- [38] P. Fan, D. Gu, G.-X. Liang, J.-T. Luo, J.-L. Chen, Z.-H. Zheng, D.-P. Zhang, High-performance perovskite CH₃NH₃PbI₃ thin films for solar cells prepared by single-source physical vapour deposition, *Sci. Rep.* 6 (2016) 29910.
- [39] Y. Zhao, C. Li, J. Jiang, B. Wang, L. Shen, Sensitive and stable tin-lead hybrid perovskite photodetectors enabled by double-sided surface passivation for infrared upconversion detection, *Small* 16 (2020) 2001534.
- [40] S. Qiao, Y. Liu, J. Liu, G. Fu, S. Wang, High-responsivity, fast, and self-powered narrowband perovskite heterojunction photodetectors with a tunable response range in the visible and near-infrared region, *ACS Appl. Mater. Interfaces* 13 (2021) 34625–34636.
- [41] J.-J. Wang, C. Fu, H.-Y. Cheng, X.-W. Tong, Z.-X. Zhang, D. Wu, L.-M. Chen, F.-X. Liang, L.-B. Luo, Leaky mode resonance-induced sensitive ultraviolet photodetector composed of graphene/small diameter silicon nanowire array heterojunctions, *ACS Nano* 15 (2021) 16729–16737.
- [42] M. Patel, P.M. Patanya, V. Patel, C.K. Sumesh, D.J. Late, Large area, broadband and highly sensitive photodetector based on ZnO-WS₂/Si heterojunction, *Sol. Energy* 206 (2020) 974–982.
- [43] R. Ramadan, V. Torres-Costa, R.J. Martín-Palma, Self-powered broadband hybrid organic-inorganic photodetectors based on PEDOT:PSS and silicon micro-nanostructures, *J. Mater. Chem. C* 9 (2021) 4682–4694.
- [44] H. Mondal, S.K. Ray, P. Chakrabarty, S. Pal, G. Gangopadhyay, S. Das, S. Das, R. Basori, High-performance chlorophyll-b/Si nanowire heterostructure for self-biasing bioinorganic hybrid photodetectors, *ACS Appl. Nano Mater.* 4 (2021) 5726–5736.
- [45] C.W. Jang, D.H. Shin, S.-H. Choi, Remarkable noise reduction in high-stability self-powered doped graphene/Si-quantum dot broadband photodetectors by using graphene quantum dots as an interlayer, *ACS Sustain. Chem. Eng.* 10 (2022) 9872–9878.
- [46] F. Bai, J. Qi, F. Li, Y. Fang, W. Han, H. Wu, Y.A. Zhang, High-performance self-powered photodetector based on monolayer MoS₂/perovskite heterostructures, *Adv. Mater. Interfaces* 5 (2018) 1701275.
- [47] C. Ma, Y. Shi, W. Hu, M.-H. Chiu, Z. Liu, A. Bera, F. Li, H. Wang, L.-J. Li, T. Wu, Heterostructured WS₂/CH₃NH₃PbI₃ photoconductors with suppressed dark current and enhanced photodetectivity, *Adv. Mater.* 28 (2016) 3683–3689.
- [48] J. Lu, J.A. Carvalho, H. Liu, S.X. Lim, A.H.C. Neto, C.H. Sow, Hybrid bilayer WSe₂-CH₃NH₃PbI₃ organolead halide perovskite as a high-performance photodetector, *Angew. Chem. Int. Ed.* 55 (2016) 11945–11949.
- [49] B. Sun, S. Xi, Z. Liu, X. Liu, Z. Wang, X. Tana, T. Shia, J. Zhou, G. Liao, Sensitive, fast, and stable photodetector based on perovskite/MoS₂ hybrid film, *Appl. Surf. Sci.* 493 (2019) 389–395.
- [50] J. Ghosh, L.P.L. Mawlong, G.B. Manasa, A.J. Pattison, W. Theis, S. Chakraborty, P.K. Giri, Solid-state synthesis of stable and color tunable cesium lead halide perovskite nanocrystals and the mechanism of high-performance photodetection in a monolayer MoS₂/CsPbBr₃ vertical heterojunction, *J. Mater. Chem. C* 8 (2020) 8917–8934.
- [51] F. Fang, Y. Wan, H. Li, S. Fang, F. Huang, B. Zhou, K. Jiang, V. Tung, L.-J. Li, Y. Shi, Two-dimensional Cs₂AgBiBr₆/WS₂ heterostructure-based photodetector with boosted detectivity via interfacial engineering, *ACS Nano* 16 (2022) 3985–3993.
- [52] C. Fang, H. Wang, Z. Shen, H. Shen, S. Wang, J. Ma, J. Wang, H. Luo, D. Li, High-performance photodetectors based on lead-free 2D Ruddlesden-Popper perovskite/MoS₂ heterostructures, *ACS Appl. Mater. Interfaces* 11 (2019) 8419–8427.

- [53] Y. Tang, M. Liang, M. Zhang, A. Honarfar, X. Zou, M. Abdellah, T. Pullerits, K. Zheng, Q. Chi, Photodetector based on spontaneously grown strongly coupled MAPbBr₃/N-rGO hybrids showing enhanced performance, *ACS Appl. Mater. Interfaces* 12 (2020) 858–867.
- [54] F. Li, Z. Qiu, S. Liu, H. Zhang, Carbon nanotube-perovskite composites for ultra-sensitive broadband photodiodes, *ACS Appl. Nano Mater.* 2 (2019) 4974–4982.
- [55] L.-H. Zeng, Q.-M. Chen, Z.-X. Zhang, D. Wu, H. Yuan, Y.-Y. Li, W. Qarony, S.P. Lau, L.-B. Luo, Y.H. Tsang, Multilayered PdSe₂/perovskite Schottky junction for fast, self-powered, polarization-sensitive, broadband photodetectors, and image sensor application, *Adv. Sci.* 6 (2019) 1901134.
- [56] T. Zhu, Y. Yang, L. Zheng, L. Liu, M.L. Becker, X. Gong, Solution-processed flexible broadband photodetectors with solution-processed transparent polymeric electrode, *Adv. Funct. Mater.* 30 (2020) 1909487.
- [57] L. Dou, Y. Yang, J. You, Z. Hong, W.-H. Chang, G. Li, Y. Yang, Solution-processed hybrid perovskite photodetectors with high detectivity, *Nat. Commun.* 5 (2014) 5404.